Nonlinear two-fluid modeling of plasma response to RMPs for the ELM control in the ITER baseline

Q.M. Hu[1], J.-K. Park[1], N.C. Logan[2], S.M. Yang[1], B.A. Grierson[1], R. Nazikian[1], and Q. Yu[3]

[1] Princeton Plasma Physics Laboratory, Princeton, NJ 08543-0451, USA

[2] Lawrence Livermore National Laboratory, 7000 East Ave, Livermore, CA 94550, USA

[3] Max-Plank-Institut fur Plasmaphysik, 85748 Garching, Germany

E-mail: qhu@pppl.gov

Abstract

Numerical modeling, combining the toroidal ideal MHD code GPEC and the nonlinear two-fluid MHD code TM1, was used for comprehensive studies of the plasma response to resonant magnetic perturbations (RMPs) with toroidal mode number n = 1-5 for controlling edge-localized modes (ELMs) in ITER for the standard operation scenario (15 MA Q = 10). Several issues related to RMP ELM control are investigated, including the optimization of the RMP coils configuration, the evaluation of the magnitude of density pump-out and the q_{95} windows of ELM suppression. GPEC calculates the magnetic response, which consistently includes the very important edge kink/peeling response to static magnetic perturbations. GPEC two-dimensional scans of the relative coil current phasing among the three rows of internal coils, at fixed coil current amplitude, reveal the optimal phasing for the RMP coil configuration with n = 1- 5, respectively. The poloidal half wavelength of resonant mode at the edge of plasma calculated by GPEC indicates that the midplane row coils have the best resonant coupling with the plasma for n = 2, while the upper and lower row coils have the best resonant coupling with the plasma for n = 3. Based on the plasma kinetic equilibrium and the GPEC calculations of the magnetic response, TM1 was used to simulate the conditions for RMP field penetration in the ITER pedestal. TM1 shows magnetic island formation at the foot of ITER pedestal with RMP coil current threshold ranging from 4 kAt to 8 kAt with n = 2 to 4. These magnetic islands at the pedestal-foot lead to density pump-out, the magnitude of which scales as $I_{\mathrm{RMP}}^{0.5}$ and ranges from 5% to 20% at the pedestal-top when scanning the coil current from 4 to 60 kAt. The density pump-out is found to be weaker for higher n RMP. The nonlinear TM1 simulations also show field penetration at the pedestal-top, where the threshold of RMP coil current depends on the q_{95}. The alignment of the magnetic island and the location of the pedestal-top decreases the height and width of the pedestal to suppress ELMs. Simulations by two-dimensional scans of RMP coil current and q_{95} reveal the accessible q_{95} windows of ELM suppression for both n = 3 and 4 RMPs. The predicted q_{95} windows of ELM suppression are very similar to the ones in currently operating tokamaks and the required RMP coil current for ELM suppression is less than 40-50 kAt, which is well within the designed capability for ITER. In addition, the simulations indicate that wide q_{95} windows of ELM suppression may be accessible in ITER by operating with dominant n = 4 (or n = 5) RMPs.

Keywords: Resonant Magnetic Perturbations (RMPs), density pump-out, ELMs suppression

1. Introduction

The periodic and transient power load onto the plasma-facing components caused by type-I edge-localized modes (ELMs) in high performance H-mode plasmas [1] is a critical issue for the integrity and lifetime of these components in future high power H-mode devices, such as the International Tokamak Experimental Reactor (ITER) [2]. Effective control of the ELMs is an essential issue for the operation of fusion devices such as ITER [3]. One method to control ELMs is the use of resonant magnetic perturbations (RMPs) [4], which was first demonstrated in DIII-D with complete ELM suppression [4–7] and then widely applied in tokamaks worldwide [8–13]. The successful full suppression of ELMs in multiple tokamaks [6,7,11–16] increased the confidence for RMP ELM suppression in ITER [3].

Along with the demonstration of RMP-ELM suppression in tokamaks worldwide, the constraints of access conditions are well documented. (1) It is commonly observed that full ELM suppression can be achieved only for specific edge safety factor q_{95} range ($q_{95} \sim m/n$) by RMPs with n = 2 and 3 in DIII-D [6,7,17–19], n =1 and 2 in KSTAR [16,20–22], n = 2 in ASDEX-Upgrade (AUG) [23], and n = 1, 2 and 3 in EAST [13,24,25]. Here, m and n are the poloidal and toroidal mode numbers. (2) An upper bound exists on the pedestal density (with $n_{\mathrm{e,ped}}/n_{\mathrm{G}}<0.5$) to access complete ELM suppression in both DIII-D [26,27] and AUG [23], (3) and a lower bound of toroidal rotation is also observed in DIII-D to access ELM suppression [27]. (4) ELM suppression is found to be sensitive

to the triangularity of the plasma shape in both AUG [23,28] and DIII-D [27]. (5) The applied RMPs usually produce enhanced particle transport (called density pump-out, with pedestal density reduced up to 50%) [6,7] and confinement degradation. The mechanism determining these constraints of access conditions needs to be addressed to strengthen the physics basis for predicting reliable and robust ELM suppression in ITER.

Various mechanisms have been proposed to explain the phenomenology of RMP effects on the H-mode pedestal, including the role of magnetic stochasticity in pedestal transport [4,29–31], key role of edge kink/peeling response in ELM suppression [32–39], coupling to ballooning modes in ELM mitigation and suppression [40,41], turbulence effects on edge transport [14,42,43], magnetic island formation due to resonant field penetration in the edge rational surfaces [6,13,14,44–48], and non-ambipolar transport modifying the edge electric field [49]. It is most likely that all these mechanisms are involved in the RMP ELM suppression and density pump-out, but nonetheless it is very important to construct a predictive model that can (a) reproduces much of the phenomenology and parametric trends in the existing data, and (b) provides a physics basis to predict ELM suppression and pump-out in low-collisionality ITER high fusion power plasmas.

To date several criteria/models have been developed to predict ELM suppression: (1) vacuum island overlap width (VIOW) model based on vacuum magnetic field calculation shows quantitative agreement of the RMP coil current threshold for ELM suppression in DIII-D [29], and it is also used to predict the required RMP current for ITER ELM control [50]. (2) Linear response modeling by MARS-F code established two criteria [51] from several tokamaks, which can be used to optimize the RMP coil current configuration. One is the resonant radial magnetic field perturbation amplitude at the rational surface close to the plasma boundary, and the other is the computed normal displacement of the plasma boundary surface near the X-point. (3) Edge resonant overlap field criteria [16] established by GPEC code [52] mainly for KSTAR tokamak, which accounts for both the edge kink-peeling and vacuum field, can also be potentially used to optimize the RMP coil current configuration. (4) Resonant field penetration model in the pedestal by TM1 code (numerical) [45,53] and EPEC code (analytical) [47,48]. It has been well validated that MARS-F and GPEC can predict the global MHD plasma magnetic response very well, while they can't predict the nonlinear MHD physics and exact RMP coil current required for ELM suppression. In the highly nonlinear, rapidly flowing and highly conducting plasma in the pedestal, penetration of the applied RMPs should be much weaker than for vacuum or highly resistive calculations, while the local RMP penetration on edge rational surfaces is a leading contender to explain the pedestal bifurcation into the ELM-suppressed state [13,14,18,54]. The nonlinear modeling of island formation [19,44–46] by TM1 for experimental values of collisionality, resistivity and cross-field transport has demonstrated agreement with the key trends observed in experiments including the ubiquitous upper bound on density [23,27] and the lower bound on toroidal rotation [27] to access ELM suppression, the narrow isolated and overlapping q_{95} windows [7] of ELM suppression, and the preservation of the edge-transport-barrier (ETB) [6] during density pump-out and ELM suppression. Therefore, the integration of the linear and nonlinear models will enhance the capability of predicting ELM suppression in ITER, which motivates the work presented in this paper.

This paper presents the prediction of plasma response for ELM control in ITER for the Q = 10 standard operating scenarios by using GPEC and TM1. It is organized as follows: the ideal magnetic response calculated by GPEC is shown in section 2 for the purpose of optimizing the RMP coil configuration as well as providing 3D magnetic boundary conditions for TM1 simulations. In section 3.1, nonlinear TM1 simulations of the density pump-out by n = 2, 3 and 4 RMP are presented. Section 3.2 shows the TM1 simulations of q_{95} windows versus RMP coil threshold for ELM suppression by n = 3 and 4 RMP. A discussion and summary of the model and results are given in section 4.

2. Plasma response calculation by GPEC

In this work, we use the high-current ITER standard operating scenario [50,55] plasma equilibrium as the target: I_p = 15 MA, Q = 10, B_t = 5.3 T, q_{95} = 3.14. Figure 1(a) shows the shape of the plasma with a cross-section of the poloidal flux surface. The radial profiles of safety factor q, plasma current density, electron density n_e and temperature T_e are shown in figure 1(b) and (c). It is well known that plasma rotation is important in both the plasma response and determining access to ELM suppression. Here, we choose the toroidal rotation profile with Pr = 0.3 and τ_Φ/τ_E=1 according to previous studies [55,56] as shown in figure 1(d). Here, the Prandtl number Pr is the ratio of the toroidal momentum diffusivity to thermal diffusivity, while τ_Φ and τ_E are the toroidal momentum and thermal confinement time, respectively. Figure 1(d) also displays the profiles of $\mathbf{E}\times\mathbf{B}$ frequency, which includes both the contribution of toroidal rotation and ion pressure gradient.

The ELM control coils in ITER are located at the low field side of the torus (figure 1(a)), consisting of three toroidal rows, with nine coils in each row. The upper and lower row coils are centered at $\Phi_j = 30° + 40°j$ (j = 0–8) along the toroidal angle, with each coil spanning 29.4° toroidal angle for the upper row and 30.5° for the lower row [50,55]. The middle row coils are centered at $\Phi_j = 26.7° + 40°\ j$ (j = 0–8), each spanning 20.9° toroidal angle. The relative (small) shift of the coils toroidal locations between the upper (lower) and middle rows naturally introduces a phase shift of the applied coil currents, for a given toroidal component. Even larger toroidal phase shift can be created between these three rows of coils, by choosing different coil current distributions along the toroidal angle. With 27 independent power supplies, these coils can generate external magnetic perturbation fields with various toroidal mode numbers. In this section, we will consider n = 1, 2, 3, 4 and 5 and vary the relative phase of the current in the different coil rows, referred to as 'coil phasing', for the purpose of

providing the optimal phasings for the coupling of each toroidal mode number.

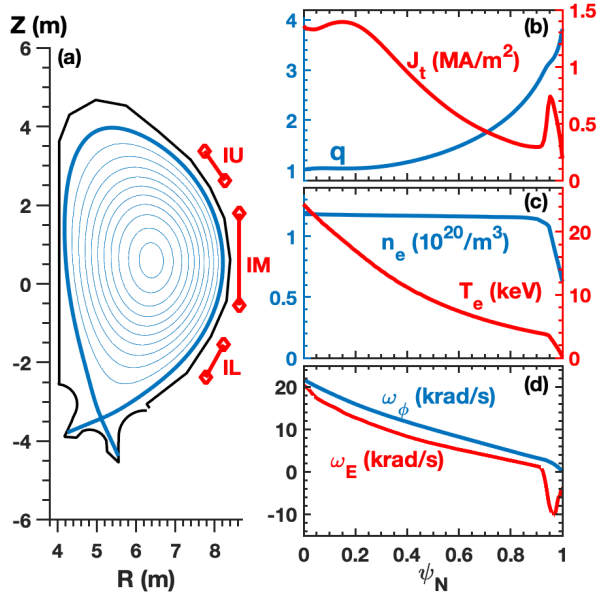

Figure 1. Equilibrium and profiles for ITER Q=10 15MA standard operating scenario in terms of (a) cross-sections of plasma shapes, profiles of (b) safety factor q and toroidal current density J_t, (c) electron density n_e and temperature T_e, (d) toroidal rotation and **E**×**B** frequency.

The 3D field that matches the field line pitch at the outer rational magnetic surfaces is called the resonant field and is known to drive magnetic islands when it is strong enough [57]. The resonant field calculated by the Generalized Perturbed Equilibrium Code (GPEC) [52] takes into account the ideal MHD plasma response to applied 3D fields. The total "effective resonant field" in a GPEC perturbed equilibrium includes both the ideal plasma response and the applied vacuum field [58,59], and it is generally very different from the vacuum resonant field due to the plasma response [32–39]. In GPEC, the resonant component of the 3D field for m and n is calculated based on the coordinate independent flux rather than by the coordinate dependent spectral amplitude of the perturbed field [60], and it can be represented by [61]

$$\delta B_{mn}=\frac{\oint(\delta\vec{B}\cdot d\vec{a})e^{i(m\vartheta-n\varphi)}}{\oint da}, \quad (1)$$

where da is the surface area element at each rational surface, and (ϑ, φ) are the poloidal and toroidal angle in the chosen magnetic coordinate system. Note that this coordinate independent resonant harmonics can only be defined in straight-field-line coordinates. In the presence of multiple rational surfaces (which is common in tokamaks), it is useful to write the resonant field as vector by

$$\vec{B}=\{\delta B_{mn}|q(0<\psi_N<1)=m/n\}, \quad (2)$$

where q is the safety factor and ψ_N is the normalized poloidal flux.

The resonant field can be represented with the Fourier decomposed external field at the plasma boundary and coupling matrix. We used coordinate independent mode, using extra weighting factor based on the area norm on the boundary surface [62,63]. This gives a coupling matrix and given vector by

$$\vec{B}=\overleftrightarrow{C}\cdot\vec{V}_b^x, \quad (3)$$

The $\vec{V}_b^x$ is given with both the resonant and non-resonant harmonics V_{bmn}^x,

$$\vec{V}_{bmn}^x=\frac{\oint w^{1/2}(\delta\vec{B}^x\cdot d\vec{a})e^{i(m\vartheta-n\varphi)}}{\sqrt{\oint \mathrm{da}}}, \quad (4)$$

Where $w=1/J|\vec{\nabla}\psi|$ and $J=(\vec{\nabla}\psi\cdot\vec{\nabla}\vartheta\times\vec{\nabla}\varphi)^{-1}$. The coupling matrix $\overleftrightarrow{C}$ defined between $\vec{B}$ and $\vec{V}_b^x$ is easily calculated from GPEC calculations. The coupling matrix $\overleftrightarrow{C}$ has dimensions R×M, where R is the number of rational surfaces included and M is the number of poloidal harmonics of the external magnetic field on the boundary. By singular value decomposition (SVD), it is possible to truncate the full coupling matrix $\overleftrightarrow{C}$. For example, $\overleftrightarrow{C}_C$ (ψ_N<0.9) and $\overleftrightarrow{C}_E$ (ψ_N>0.9) represent the core and edge, and $B_C=\overleftrightarrow{C}_C\cdot\vec{V}_b^x$ and $B_E=\overleftrightarrow{C}_E\cdot\vec{V}_b^x$separates the core and edge dominant resonant field, respectively. Furthermore, $\delta B_C = (\sum|B_{C,mn}|^2/N)^{1/2}$ and $\delta B_E = (\sum|B_{E,mn}|^2/N)^{1/2}$ represent the core and edge RMP strength (overlap resonant field) respectively, and N is the number of rational surfaces in the core or edge region.

The plasma response calculated by GPEC has been benchmarked through other MHD codes such as MARS-F [64] and validated by experiment [36,62,65]. GPEC successfully predicts the ELM suppression window without core locked modes in the 3D coil phase space [16] based on the requirement that the edge overlap field is higher than the threshold for ELM suppression while the core overlap field is below the threshold for triggering core locked modes. The physical understanding behind this success is that ELM suppression is believed to be a consequence of resonant field penetration at the pedestal-top [44,45]. Recently, the capability of GPEC enables multi-purpose optimization of RMP spectrum [66], i.e. for error field correction [67,68] by optimizing the core overlap field for ELM control by maximizing edge overlap field and minimizing the core overlap field to lower the risk of core locked modes [61], and for neoclassical toroidal viscosity (NTV) torque rotation control.

Building on these benchmarked successes in plasma response modeling, the edge overlap field calculated by GPEC is used here to investigate the optimal coil phasing for the ITER standard operation scenarios for n = 1 to 5. For each n, complex representations for the coil current in the upper, middle and lower rows are assumed as $I^U\exp(i\Phi^U)$, $I^M\exp(i\Phi^M)$ and $I^L\exp(i\Phi^L)$, respectively. The coil currents are assumed to be the same $I^U=I^M=I^L$, which simplifies the scanning to 2D parameter space ($\Delta\Phi_{UM}$, $\Delta\Phi_{LM}$) based on linear combination of the magnetic response from the 3 rows. Here, $\Delta\Phi_{UM} = \Phi^U-\Phi^M$ and $\Delta\Phi_{LM}= \Phi^L-\Phi^M$.

Edge truncation is used in GPEC to avoid the numerical issue around the separatrix. Optimal truncation is used in GPEC to (1) make sure the equilibrium at the truncation location is ideally stable by checking the total energy of the least stable mode after the last rational and ending integration

at the first local maximum, and (2) include as more rational surfaces as possible. Note that (1) avoids erroneous physics of associated with external kink instabilities and (2) is limited by the resolution of the EFIT equilibrium in the edge (in practice, the Grad-Shafronov equilibrium starts to break down when pushing too far out toward the separatrix). For the results presented in this paper, the truncation location is chosen at ψ_N =0.992-0.998 for n = 1-5, which includes all the rational surfaces and the calculated edge resonant field changes little when changing the truncation location in this region.

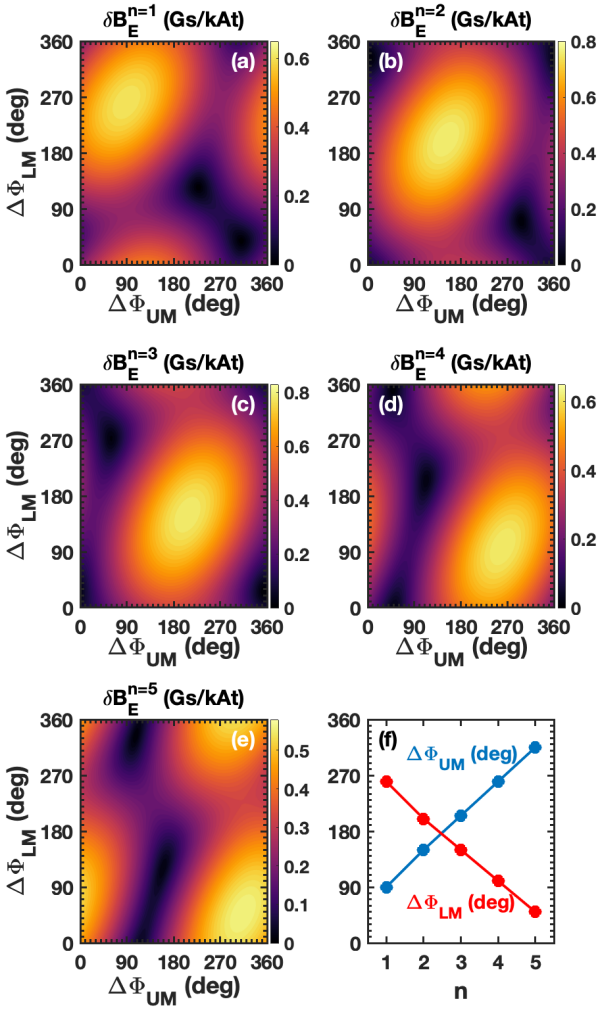

Figure 2. The GPEC calculated edge overlap field versus $\Delta\Phi_{UM}$ and $\Delta\Phi_{LM}$ for (a) n = 1, (b) n = 2, (c) n = 3, (d) n = 4, and (e) n=5 coil configurations. (f) The optimal coil phasing of $\Delta\Phi_{UM}$ and $\Delta\Phi_{LM}$ are shown versus toroidal mode number n. Here, the same coil current amplitude of 45 kAt in all three rows (IU, IM, IL) is applied for the ITER 15 MA inductive plasma. Here, $\Delta\Phi_{UM}$ and $\Delta\Phi_{LM}$ are the phase difference between I^U and I^M, and I^L and I^M, respectively.

Figure 2 shows the calculated results of such 2D scans in terms of edge overlap (ψ_N>0.9) resonant field δB_E versus $\Delta\Phi_{UM}$ and $\Delta\Phi_{LM}$ for n = 1, 2, 3, 4 and 5. It shows that there is an optimal coil phasing in the ($\Delta\Phi_{UM}$, $\Delta\Phi_{LM}$) space for each n, yielding the maximum amplitude of edge resonant field. The optimal phase for each n is listed in table 1 and shown in figure 2(f), at which the 3D field will be most efficient to generate a strong enough edge resonant field to suppress ELMs. Interestingly, the optimal $\Delta\Phi_{UM}$ linearly increases with increasing n, while $\Delta\Phi_{LM}$ linearly decreases with n. Notably, the optimal coil phasing for n =1-4 from GPEC is very similar to that from MARS-F modeling in terms of X-point displacement (figure 12 in Ref. [55]).

Table 1. The optimal coil phasing of edge overlap field for n = 1, 2, 3, 4 and 5.

	n = 1	n = 2	n = 3	n = 4	n = 5
$\Delta\Phi_{UM}$	90°	150°	205°	260°	315°
$\Delta\Phi_{LM}$	260°	200°	150°	100°	50°

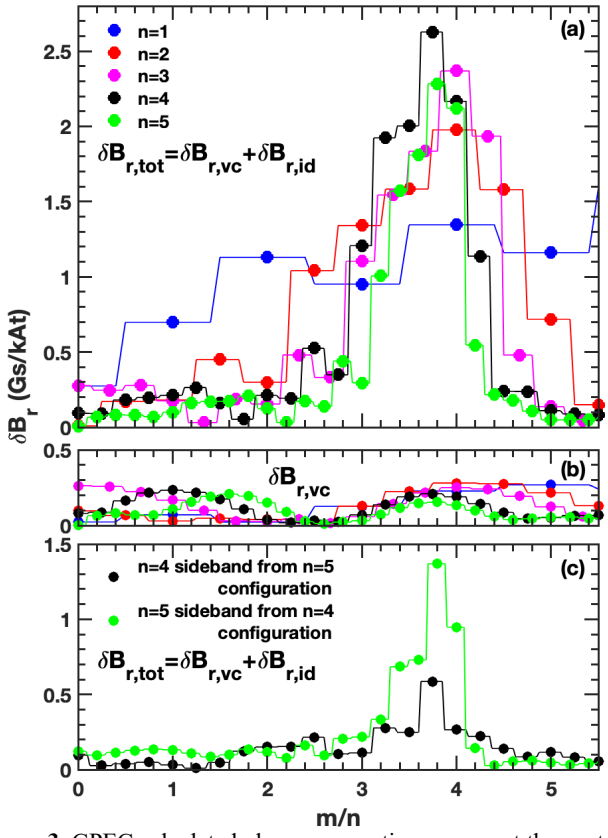

Figure 3. GPEC calculated plasma magnetic response at the control surface with the optimal coil phasing for different toroidal mode numbers, shown are the poloidal spectrum of (a) the total of magnetic response $\delta B_{r,tot}$ and (b) the vacuum field $\delta B_{r,vc}$. (c) Shown are the n = 4 and 5 sideband $\delta B_{r,tot}$ from the optimal n = 5 and 4 configurations, respectively

Previous simulations by combining GPEC and TM1 show good agreement and high numerical efficiency in explaining ELM suppression observed in the DIII-D and KSTAR experiments [19,44–46]. The nonlinear TM1 simulation uses the 3D magnetic boundary conditions from GPEC at the plasma edge surface (ψ_N = 1). The poloidal spectra of the resonant field amplitude at the plasma boundary are shown in figure 3 by using the optimal coil phasing at each n. Compared to the vacuum field $\delta B_{r,vc}$ shown in figure 3(b), the total of the

resonant field $\delta B_{r,total}$ (including both the vacuum $\delta B_{r,vc}$ and ideal MHD magnetic response $\delta B_{r,id}$) in figure 3(a) clearly shows the amplification effect due to the edge kink-peeling response [33,36,37]. Figure 3(a) also shows that, for those components that resonate in the pedestal region ($3 \leq m/n \leq 3.7$), the amplitudes of resonant fields are very close for n = 2-5. In the next section, TM1 simulation of resonant field penetration will use $\delta B_{r,total}$ from figure 3(a) as the 3D magnetic boundary conditions.

It should be noted that there is n = 5 (n = 4) sideband due to one more (one less) coil for the n = 4 (n = 5) configuration, as illustrated in figure 4(c) for the optimal configuration. According to GPEC calculation, the amplitude of the n = 5 sideband edge resonant field from the dominant n = 4 configuration is about half of the n = 4 edge resonant field. However, for the dominant and optimal n = 5 configuration, the amplitude of the n = 4 sideband edge resonant component is much weaker. The sideband effect will lead to mixed n = 4 and 5 resonant fields, the effects of which is discussed in the next section.

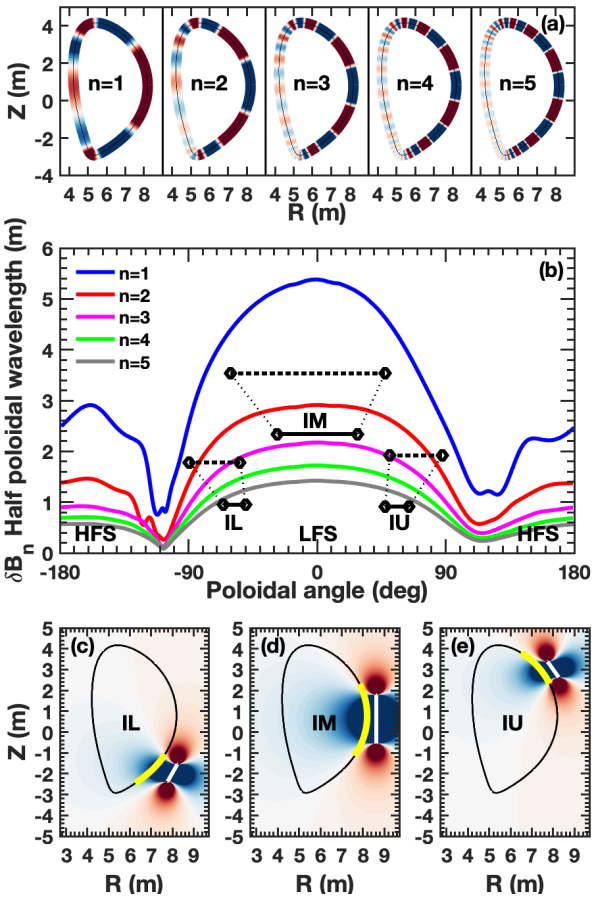

Figure 4. (a) Dominant mode structure for the edge plasma response, (b) GPEC calculated poloidal half wavelength at the control surface for n = 1-5, and radial vacuum magnetic field generated by (c) IL, (d) IM and (e) IU coils separately. Here, the actual (black solid) and effective (black dotted) coil width for the IL, IM and IU are overlapped in figure 4(b), and the effective coil width is determined by the length of the yellow curves shown in Fig. 4(c-e), the actual coil width is shown in white line as well.

. The coupling matrix $\boldsymbol{C}$ in Eq. (4) calculated by GPEC provides unique insights to examine the resonant coupling between 3D coils and the plasma. This coupling matrix is positive definite, and decomposing it using SVD gives R positive singular values. These singular values rank the corresponding unit right singular vectors (RSVs) of external flux by the Euclidean norm of the edge resonances. The first of these RSVs usually has a singular value much larger than the others and dominates the total resonant drive in tokamak [61,66]. This first RSV structure has been called the "dominant mode" of external flux. Figure 4(a) shows the edge dominant mode structures for n = 1-5. Here, the dominant mode is the unit magnitude vector translated to the poloidal angle by inverse Fourier transformation (IFT), and the cross-section plots show the IFT along the plasma boundary at a fixed toroidal angle of 0. The dominant mode has a persistent region of high amplitude and long wavelength on the low field side (LFS) of the machine (which is why 3D coils built in this region are so successful [66]). The poloidal half wavelength of the dominant mode (half the inverse of the derivative of the toroidal phase as a function of the poloidal length along the plasma surface) is plotted against the cylindrical poloidal angle taken about the nominal major radius of ITER, as shown in figure 4(b) for n = 1-5. It is clear that the dominant mode half wavelength for each n decays quickly when it moves away from the LFS midplane. The poloidal half wavelength on the LFS midplane decreases from 5.4 m to 1.4 m when increasing n from 1 to 5 due to higher poloidal mode number. The actual and effective widths of the 3 rows coils are also plotted in figure 4(b) by black solid lines and black dotted lines. Here, the poloidal range of the radial magnetic field generated by the 3D coils will expand when it is away from the coils, leading to expanded effective width as illustrated in figure 4(c-e) for IL, IM and IU coils, respectively. The effective width is determined by the interface of the radial magnetic field with the plasma surface as marked in yellow. The resonant coupling between the coil and the plasma is better when the effective coils width at the plasma surface is close to the poloidal half wavelength. According to the comparison between the effective width of the 3D coils in ITER and the poloidal half wavelength of the edge dominant mode, IM is expected to have its best resonant coupling for n = 1-2, while IU and IL will have their best resonant coupling for n = 2-3.

3.Two-fluid nonlinear modeling

In this section, TM1 code [53,69,70] is used to simulate the nonlinear resonant field penetration and the associated enhanced collisional transport in the pedestal of ITER. For our analysis we use the TM1 code, which has recently been improved to perform high-resolution simulations with multiple helical boundary conditions relevant to the DIII-D pedestal. TM1 is a nonlinear time-dependent two-fluid MHD code with cylindrical geometry and circular cross-section. TM1 includes the nonlinear coupling of harmonics of each helicity, and it solves the two-fluid MHD equations, including the generalized Ohm's law, the motion equation in the parallel

and perpendicular direction, the continuity equation and the energy transport equation [45,53,69,70]. Specifically, it solves the motion equation by evaluating the torque balance between the electromagnetic (**J**×**B**) torque due to the RMP and the plasma viscosity in the motion equation (see details in the Appendix of Ref. [45]). Torque balance governs the bifurcation from screening to penetration of resonant fields in the pedestal, which is also sensitive to diamagnetic drifts through Ohm's law. The electron density and temperature are self-consistently evaluated through the electron continuity equation and the energy transport equation. Physically, RMP enhances parallel transport across the formed magnetic island or screening current, leading to enhanced particle and thermal transport across rational surfaces [53,71]. The temperature dependent neoclassical resistivity is utilized in the simulation to take into account the neoclassical effect in toroidal geometry. The enhanced collisional particle and thermal transport are solved self-consistently with the penetration and/or screening of resonant fields in the TM1 code. Dedicated numerical methods are utilized in TM1 to reduce the numerical error associated with large values of the magnetic Reynolds number S and $\chi_{\parallel}/\chi_{\perp}$ [72]. In addition, the radial grid size of 3200 is used to obtain high resolution simulation in the pedestal.

The cylindrical geometry utilized in the TM1 model is different from the toroidal strongly shaped geometry in the ITER plasmas. The application of the full toroidal GPEC (as introduced in section 2) includes the effects of shape and geometry in the ideal plasma response [52], which minimizes the discrepancy in the 3D magnetic boundary. In this section, only the n = 2-4 RMP amplitude at the plasma edge from the optimal coil phasing is used for the TM1 nonlinear simulations. Furthermore, in the nonlinear modeling, the small and separate magnetic islands in the pedestal region are expected to cause only a weak mode coupling effect with toroidal geometry [73]. In addition, the TRANSP code [74,75] is used to infer the transport coefficients, including the momentum, particle and thermal diffusivities, from the profiles according to the calculations of power and particle balance. They are derived to be $\mu_{\perp}= \chi_{\perp}= 3D_{\perp}= 0.4$ m^2/s at the pedestal-top, 0.1 m^2/s in the steep pedestal region, and 0.5 m^2/s at the foot of pedestal.

Previously, TM1 nonlinear two-fluid MHD simulations have shown that island formation at the top of the pedestal is quantitatively consistent with the onset of ELM suppression, while island formation at the foot of the pedestal is quantitatively consistent with density pump-out due to the enhanced parallel transport across the islands [44,45]. The TM1 simulations well-captured the fast-timescale (~ms) variations at the threshold of ELM suppression, including nonlinear bifurcations of the plasma flow, together with changes of the non-axisymmetric magnetic field structure observed in DIII-D [14,36]. Recent TM1 simulations also well predicted the q_{95} windows of ELM suppression in DIII-D and KSTAR [19].

The understanding from these TM1 successes also provides insights that simplify the predictions for ITER ELM control. Based on these, TM1 simulations will focus mainly on the pedestal-foot resonant field penetration for predicting density pump-out and mainly simulate pedestal-top resonant field penetration to predict ELM suppression. In the following, by using the equilibrium profile (figure 1) and GPEC calculated 3D magnetic boundary conditions (figure 3), TM1 simulations are performed to predict magnetic island formation in the pedestal of ITER plasma.

3.1. Density pump-out

It is well known that RMP easily penetrates into a plasma with high resistivity [57,76], and it was expected that penetration would easily happen at the high resistivity pedestal-foot of ITER plasma. Taking n = 3 RMP for example, figure 5 shows the nonlinear evolution of pedestal (ψ_N = 0.94) density due to 11/3 magnetic island formation at the pedestal-foot driven by m/n = 11/3 RMP. In the simulation, only the 11/3 component is included since it is the most outside rational surface in the computational domain, and the 10/3 rational surface is located in the middle of the pedestal and it is hard to penetrate. The RMP coil current is set to ramp up linearly from 0 to 80 ms and kept constant at different current levels. The penetration threshold of 11/3 RMP is 5 kAt in this plasma. For 4 kAt coil current, the 11/3 RMP is shielded by the plasma as indicated by the very small magnetic island width (0.25%) in figure 5(a) and causes very weak reduction in both $n_{e,ped}$ and $T_{e,ped}$. 6 kAt RMP coil current leads to 11/3 penetration at the pedestal-foot with the saturated island width $W_{11/3}$ = 0.011ψ_N, and 3% reduction in $n_{e,ped}$ and 5% reduction in $T_{e,ped}$. Further increasing RMP coil current leads to larger magnetic island width and stronger pump-out as shown in figure 5 with 15 kAt and 25 kAt coil current.

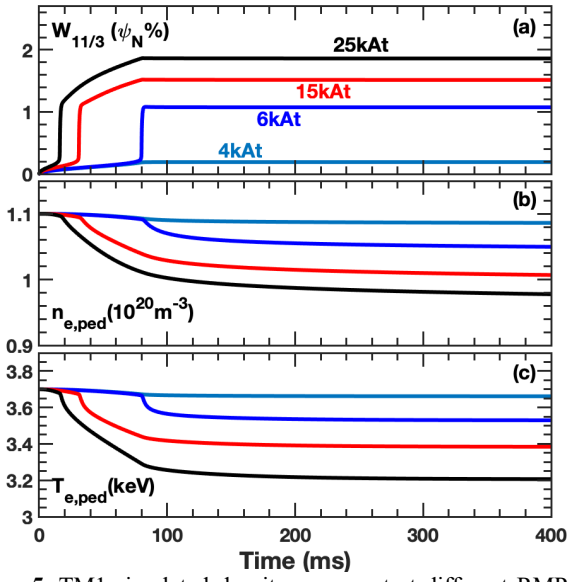

Figure 5. TM1 simulated density pump-out at different RMP coil current. Shown are time evolution of (a) 11/3 magnetic island width, (b) pedestal density and (c) pedestal temperature with I_{RMP} = 4, 6, 15 and 25 kAt.

The physics behind the reduction in both $n_{e,ped}$ and $T_{e,ped}$ is that the formation of 11/3 magnetic island at the pedestal-

foot flattens n_e and T_e profiles in the island region and lowers the global profiles due to enhanced parallel transport across the magnetic island [45,53]. Corresponding to figure 5, figure 6 shows the simulated profiles of n_e at 400 ms for those cases with different RMP coil current. It shows that, with increasing RMP coil current, the increasing magnetic island width leads to stronger and wider flattening of the n_e profiles at the pedestal-foot, resulting in stronger reduction in the profiles.

It should be noted that the reduction in n_e from TM1 simulations is due to the enhanced parallel transport, the possible additional change in turbulent or non-ambipolar transport by applied RMP is not taken into account. It is well known that the turbulence level is observed to increase following the application of RMP [42,77] and transition to ELM suppression [14]. More recent gyrokinetic simulations by XGC claim that turbulence contributes to density pump-out [78], but the simulations also show that the bulk of the pump-out arises from neoclassical transport across edge magnetic islands, which is consistent with the results from our nonlinear MHD model. According to our studies in Ref. [45], we are confident that the onset condition and parametric dependencies of ELM suppression and density pump-out is accounted for by the nonlinear MHD model without invoking turbulent transport. We take no account of such turbulence effects in the TM1 simulations on transport, and we cannot say what role, if any, the ion-scale turbulence plays in these experiments.

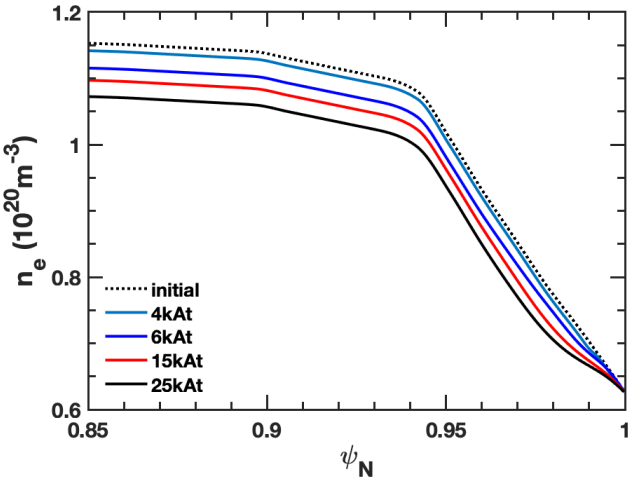

Figure 6. Corresponding to figure 5, TM1 simulated n_e profiles at different RMP coil currents. The initial profile without RMP is shown in black dotted curve.

A full scanning of the $n = 3$ RMP coil current is performed to predict the dependence of density pump-out magnitude on it, as shown by circles in figure 7 in red color. Here, the data of each point is from a single TM1 simulation after approaching its new steady state. The magnitude of density pump-out is represented by the relative change, i.e. $\Delta n_e/n_{e,ped}$, and Δn_e is the change from the initial $n_{e,ped}$ at the pedestal-top. Figure 7 shows increasing magnetic island width, and density pump-out magnitude ($\Delta n_e/n_{e,ped}$) with increasing RMP coil current. A fitting scaling of $\Delta n_e/n_{e,ped} \propto I_{RMP}^{0.5}$ is found, which is consistent with Eq. (1) in Ref. [45]. Since the pump-out magnitude linearly depends on the magnetic island width, while the island width $W \propto B_r^{0.5} \propto I_{RMP}^{0.5}$. In the DIII-D experiment, the scaling of $\Delta n_e/n_{e,ped} \propto I_{RMP}^{0.5}$ is observed according to recent analysis [79]. According to results in figure 7, 40 kAt RMP coil current will cause 13% density pump-out at the ITER pedestal-top.

TM1 predictions are also performed for n =2 and 4 as shown in figure 7 for comparison with n = 3, and m/n = 7/2 and 14/4+15/4 are the components resonating at the pedestal-foot, respectively. The threshold of RMP coil current for pedestal-foot penetration is 4.1 kAt and 7 kAt for n =2 and 4, respectively. Figure 7 shows the same scaling of density pump-out $\Delta n_e/n_{e,ped} \propto I_{RMP}^{0.5}$ for n = 2 and 4. While when the RMP coil current is strong enough to cause pedestal-foot magnetic island formation, the same RMP coil current leads to a larger magnetic island width for lower n. As a result, the same RMP coil current leads to weaker density pump-out for higher n. Taking 40 kAt for example, $\Delta n_e/n_{e,ped}$ is -17%, -13% and -7.5%, for n = 2, 3 and 4, respectively. Results in figure 7 also indicate that RMP with higher n will be more favorable for ELM control to minimize the confinement degradation prior to ELM suppression. It should be pointed out that, in the experiments due to the power balance and weaker temperature gradient at the pedestal foot, the pedestal temperature decreases little or even increases associated with density pump-out [6,7].

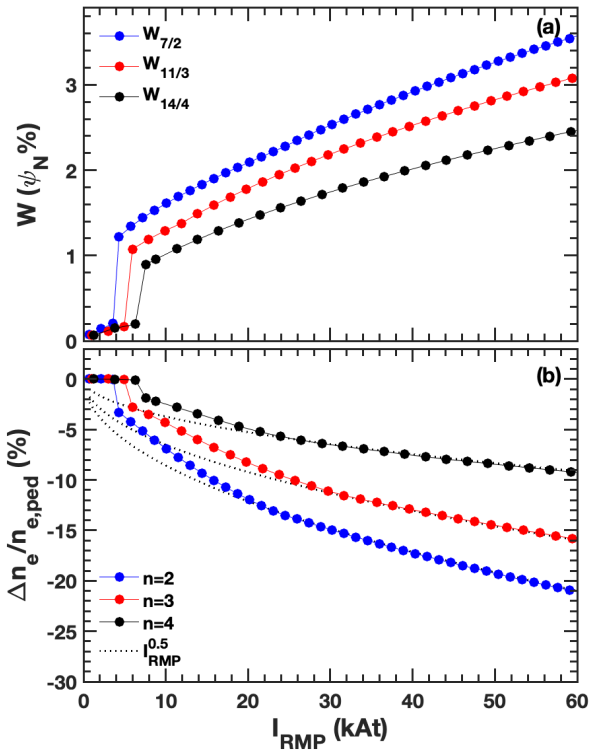

Figure 7. TM1 simulated dependence of density pump-out on RMP coil current for n = 2-4. Shown are (a) magnetic island width and (b) density pump-out magnitude $\Delta n_e/n_{e,ped}$ (in percentage) versus RMP coil current for n = 2, 3 and 4. The dotted curves in (b) indicate the $I_{RMP}^{0.5}$ fitting.

3.2. q_{95} windows for ELM suppression

In this section, TM1 modeling is performed to simulate resonant field penetration at the pedestal-top and the associated transport. Since there is only one equilibrium for the ITER standard operation scenario, the following assumptions are made to enable simulations at different q_{95}: (1) the q profile will be shifted up and down to scan q_{95}, which means constant magnetic shear at different q_{95}. (2) The boundary amplitude of the resonant field which resonates at the pedestal top changes little when q_{95} is scanned. This assumption is on the one hand based on previous GPEC calculations on DIII-D experiment; on the other hand, the range of q_{95} scanned for each resonant component is about 0.3, which will not change the magnetic response much [55]. (3) According to experience on DIII-D and KSTAR ELM control experiment, a criterion of 15% reduction in pedestal height [19,46] will be used to determine the access threshold for ELM suppression. Besides, due to the extensive calculations, resonant field penetration at the pedestal-foot is not included in the following simulations to simplify and accelerate the calculation, which will affect the RMP coil current threshold to access ELM suppression but won't affect the range of q_{95} windows of ELM suppression [19].

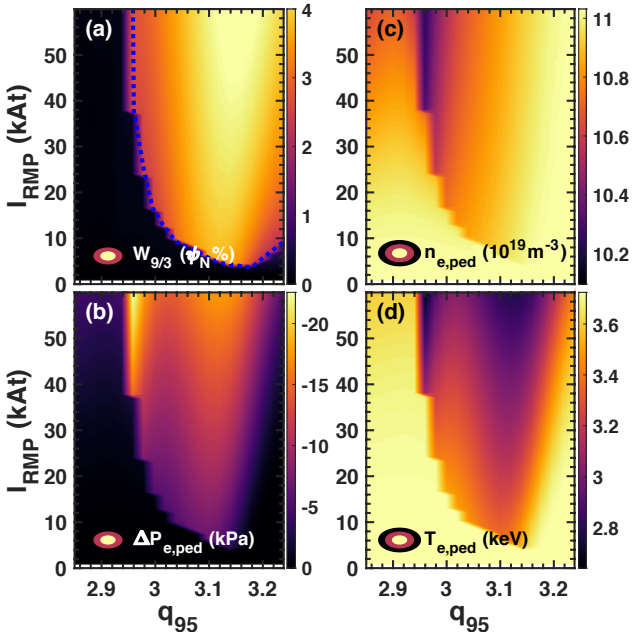

Figure 8. Simulation of the m/n = 9/3 RMP penetration and its effect on electron pressure for different q_{95}in terms of 2D contour plot of (a) magnetic island width $W_{9/3}$, (b) reduction in pedestal pressure $\Delta P_{e,ped}$, (c) pedestal density $n_{e,ped}$ and (d) pedestal temperature $T_{e,ped}$ versus q_{95} and RMP coil current.

Figure 8 shows a 2D scanning of 9/3 resonant field penetration by applying n = 3 RMP, and it includes 18 points scanning for q_{95} × 30 points scanning for I_{RMP}. The width of 9/3 island versus I_{RMP} and q_{95} in figure 8(a) clearly shows the boundary of penetration (marked by the blue dotted curve). The penetration threshold is close to zero when the perpendicular electron fluid frequency at q = 9/3 is near zero ($\omega_{\perp e}$ = 0) when q_{95} ~ 3.18. Scanning q_{95} from 2.85 to 3.18 moves the location of 9/3 rational surface inward from the steep pedestal region to the pedestal-top and faces lower and lower $\omega_{\perp e}$ at q = 9/3, resulting in a decreasing penetration threshold. In contrast, scanning upward q_{95} from 3.18 to 3.25 moves the location of 9/3 rational surface further inward and faces stronger and stronger $\omega_{\perp e}$, resulting in an increasing penetration threshold. Interestingly, when q_{95} is lower than 2.95, the 9/3 rational surface is located in the steep pedestal region, and the very strong $\omega_{\perp e}$ makes it very hard to penetrate.

The driven 9/3 magnetic island at the pedestal-top also decreases the pedestal density (figure 8(c)) and temperature (figure 8(d)) due to the same mechanism introduced in section 3.1. Due to the stronger temperature gradient at the pedestal-top compared to density gradient, 9/3 magnetic island causes more reduction in $T_{e,ped}$ as shown in figure 8(d). Reduction in $n_{e,ped}$ and $T_{e,ped}$ results in overall reduction in the pedestal electron pressure as shown in figure 8(b). As a result, the pedestal-top magnetic island limits the height and width of the pedestal to prevent its growth and suppress peeling-ballooning modes (PBM) [45,54]. However, when the 9/3 magnetic island is too far in from the pedestal-top, i.e. q_{95} = 3.25, it is hard to affect the pedestal pressure unless the island width is large enough. Figure 8 reveals that to cause strong effective reduction in pedestal pressure, it requires both that [19,46]: (1) the imposed RMP strength is sufficient to form magnetic island at the pedestal top, and (2) the rational surface of the island is in the proper radial location to cause sufficient reduction in pedestal pressure and prevent further expanding for the pedestal to be unstable for PBMs.

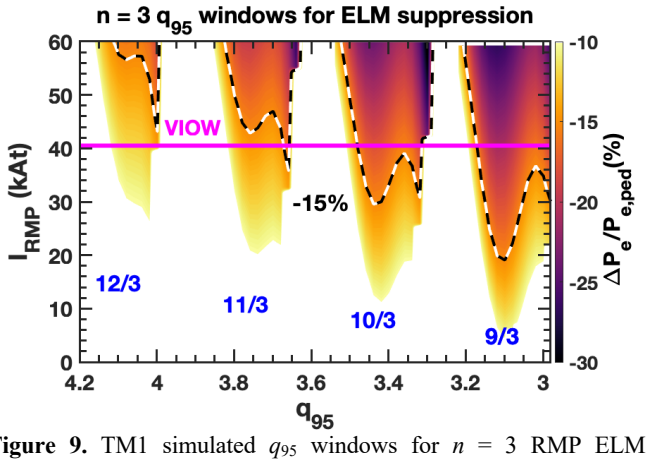

Figure 9. TM1 simulated q_{95} windows for n = 3 RMP ELM suppression in terms of pedestal pressure reduction versus q_{95} and RMP coil current I_{RMP}. The black dashed curves indicate the boundary with 15% reduction, and the purple line indicates the predicted RMP coil current for ELM suppression from the VIOW model.

It should be noted that the resonant field penetration threshold is sensitive to the plasma parameters, especially for the plasma rotation frequency. Previous scanning by TM1 simulations shows near linear dependence of the pedestal-top penetration threshold on rotation frequency [45,76], which explains the predicted lower penetration threshold in the ITER

pedestal due to low rotation frequency. The required lower penetration threshold consequently leads to low threshold of 3D coil current for ELM suppression for n = 3 as shown in figures 8 and 9.

Similar scanning simulations are performed for m/n = 10/3, 11/3 and 12/3 component RMP and the results are shown in figure 9 presented by the normalized pedestal pressure reduction $\Delta P_e/P_{e,ped}$. The black dashed curves indicate the access boundary for ELM suppression with 15% reduction in the pedestal pressure [19,46]. Figure 9 shows that different RMP components determine different q_{95} windows possibly to access ELM suppression, and the q_{95} windows of $3 < q_{95} < 3.15$, $3.3 < q_{95} < 3.45$, $3.65 < q_{95} < 3.8$ and $4 < q_{95} < 4.15$ are determined by m/n = 9/3, 10/3, 11/3 and 12/3 RMP, respectively. The required minimum RMP coil current is 20 kAt, 30 kAt, 45 kAt, and 55 kAt for 9/3, 10/3, 11/3 and 12/3 RMP to access ELM suppression, respectively, which is within the capability (maximum 90 kAt) of the 3D coils in ITER. Here, the neighboring q_{95} window differs with $\Delta q_{95} \sim 1/3$, which is determined by the toroidal mode number. The predicted n = 3 q_{95} windows for ELM suppression are very similar to both the observations and simulations in the DIII-D tokamak [19,46], except a little narrower window without overlap. The VIOW model [29] previously predicted ~40 kAt [50] of RMP coil current to access n = 3 RMP ELM suppression for the same scenario as shown by the purple line, which is about two times the TM1 prediction. This is reasonable since VIOW requires stochasticity in the ~16% ($0.84 \leq \psi_N \leq 1$) of the plasma edge, while full magnetic islands formation and overlap are not necessary from TM1 prediction.

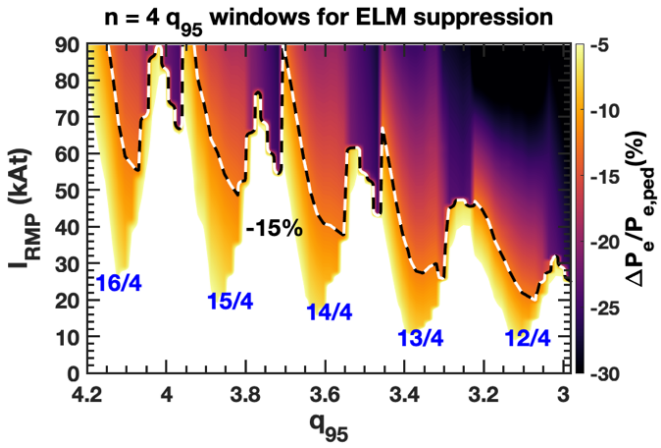

Figure 10. TM1 simulated q_{95} windows for n = 4 RMP ELM suppression in terms of pedestal pressure reduction versus q_{95} and RMP coil current I_{RMP}. The black dashed curves indicate the boundary with 15% reduction.

We also performed simulations to predict the q_{95} windows of ELM suppression for n = 4 as shown in figure 10. In the simulations, due to closer n = 4 rational surfaces at the pedestal-top, two resonant components are included for all the scanning. Multiple ELM suppression windows are predicted for each resonance from m/n = 12/4 to 16/4. Compared to n = 3 results, there is no big difference for the required RMP coil current to access ELM suppression (of course at similar q_{95} region). More importantly, figure 10 shows potentially continuous windows of ELM suppression (merger of the 12/4, 13/4 and 14/4 windows) when the RMP coil current is higher than 50 kAt with just 20-30% reduction in the pedestal pressure, which is similar to what we predict for n = 4 in DIII-D [46]. In addition, the n = 4 results in particular show that at the 90 kAt limit there may be retaining ELM suppression for a range of plasma currents from about 11-15 MA in ITER. This is in contrast to n = 3 RMPs where there are no overlapping ELM suppression windows even for much larger RMP amplitudes. Therefore, the TM1 simulations predict that the closer proximity of adjacent rational surfaces at higher-n RMP allows multiple islands to appear at the pedestal top near the RMP threshold for field penetration, producing wide q_{95} windows of ELM suppression with weak pedestal pressure reduction.

Notably, the simulations of n = 4 q_{95} windows in figure 10 do not include the effect of the n = 5 sideband resonant field. Experiment in DIII-D has confirmed that the mixed n = 2 and 3 RMPs reduced the ELM suppression threshold [80]. According to our previous simulations for mixed n = 2 and 3, we expect that the additional n = 5 sideband will enhance the n = 4 resonant field penetration in the pedestal region, and hence lower the ELM suppression threshold. In addition, we expect that, similar to n = 4, the n = 5 RMP can also lead to wide q_{95} windows of ELM suppression, although the required coil current will be higher. The n = 5 q_{95} windows and the optimal phase of 3D coils for mixed n = 4 and 5 will be explored by simulations in the future.

4. Discussion and summary

An important question is whether TM1 predictions of the particle and thermal transport from flattening across magnetic islands can be used to compare to experiments in ITER. An issue is that two-fluid TM1 simulations assume zero ion orbit width while small islands at the plasma edge may be comparable in size to the ion poloidal gyro-radius. Table 2 provides a detailed comparison of the orbit width to the predicted island width from TM1 for the top of pedestal and foot of pedestal. According to the plasma parameters, the orbit width for passing particle $\delta r = q\rho_i$ is estimated to be 2×10^{-3} m and 7.2×10^{-3} m with ion temperature of 0.25 keV and 5 keV at the foot and top of the ITER pedestal, respectively. Here, the ion Larmor radius is $\rho_i=(2m_iT_i/eB_t)^{0.5}$. We should note that recent main ion CER results demonstrate that the deuterium temperature is much closer to the electron temperature ($T_e \approx T_i \approx 0.1$ keV) near the separatrix and is well below the carbon VI temperature [81]. The poloidal orbit width for passing ions is well below the island width at both the pedestal-foot and pedestal-top. This suggests density pump-out through parallel transport should occur at the bottom of the pedestal consistent with our model, but less so at the top of the pedestal. Our model predicts the bulk of the density pump-out coming from resonant field penetration at the bottom of the pedestal (figure 6), while the reduction in the pedestal density is much weaker due to the pedestal-top island formation (figure 8).

Table 2. The island width W, passing particle orbit width δr, ion Larmor radius ρ_i at the top and bottom of ITER pedestal.

	W (cm)	δr (cm)	ρ_i (cm)
Pedestal-top	5.0	0.72	0.24
Pedestal-foot	3.0	0.2	0.05

The TM1 simulations on q_{95} windows do not include all relevant resonant components in the pedestal region, especially for n = 3 case, which may raise another important question that whether the applied RMP will trigger resonant field penetration in the steep pedestal region. Our previous simulations show possible magnetic island formation in the steep pedestal region for n = 3, but it won't cause island overlap and stochasticity [82]. Given the high sensitivity of field penetration in the pedestal to plasma parameters [45,76], an important point to consider is the effect of uncertainty in the edge pressure gradient and plasma rotation on our conclusions. The ITER edge profiles in figure 1 decay linearly, however we may anticipate a higher pressure gradient if we had instead used a Tanh function with the same pedestal width and height. This could increase the peak pressure gradient at the bottom of the E_r-well, further raising the penetration threshold in the steep gradient region. Based on the TM1 model, we anticipate that a doubling of the pressure gradient at the bottom of the E_r-well will increase the penetration threshold by ≈50%. This increase can provide a further safety margin for achieving ELM suppression while avoiding island formation in the steepest region of the ITER pedestal. However, it is also possible that the pedestal width in ITER may be larger (and the pressure gradient weaker) than estimates based on KBM (kinetic-ballooning-mode) models, due to the incomplete suppression of ITG/TEM instabilities as predicted elsewhere [83,84]. From such considerations it is clear that there are considerable uncertainties in predicting the actual edge pressure gradient and penetration threshold in ITER. Nonetheless, the clearest conclusion we can draw is that the planned capability of the ITER ELM control coils considerably exceeds our reasonable estimates for the currents required for resonant field penetration in the ITER edge.

In summary, nonlinear MHD modeling combining the GPEC and TM1 codes is carried out to predict the plasma response to RMP for ELM control in ITER during standard operation scenarios. GPEC 2D scans of the dependence of magnetic response on coil phasing obtained the optimal coil phasing to maximize the edge resonant field for ELM control for n = 1-5 configuration. Nonlinear TM1 simulations show magnetic island formation at the foot of ITER pedestal with RMP coil current threshold ranging from 4 kAt to 8 kAt for n = 2 to 4. These magnetic islands at the pedestal-foot lead to density pump-out, the magnitude of which ranges from 5% to 20% at the pedestal-top scales as $I_{RMP}^{0.5}$, and the magnitude of pump-out is weaker for higher n. The nonlinear TM1 simulations also show field penetration at the pedestal-top, and the threshold of RMP coil current depends on the q_{95}. Simulations by two-dimensional scans of RMP coil current and q_{95} reveal the accessing q_{95} windows of ELM suppression for both n = 3 and 4 RMPs. The predicted q_{95} windows of ELM suppression are very similar to the observations in recent tokamaks and the required RMP coil current is less than 40-50 kAt, which is well within the designed capability in ITER. In addition, the simulations indicate that wide q_{95} windows of ELM suppression may be accessible in ITER by operating n = 4 (or n = 5) RMPs, and high n RMP is more favorable for ELM control to minimize the confinement degradation.

ACKNOWLEDGEMENTS

The author Q. Hu appreciated Dr. Y.Q. Liu for providing the ITER equilibrium and profiles. This material is based upon work supported by the U.S. Department of Energy, Office of Science, Office of Fusion Energy Sciences, using the DIII-D National Fusion Facility, a DOE Office of Science user facility, under Awards No. DE-AC02-09CH11466, No. DE-FC02-04ER54698 and No. DE-AC52-07NA27344.

REFERENCES

[1] Wagner F et al 1982 *Phys. Rev. Lett.* **49** 1408–12
[2] Loarte A et al 2003 *J. Nucl. Mater.* **313–316** 962–6
[3] Loarte A et al 2014 *Nucl. Fusion* **54** 033007
[4] Evans T E et al 2004 *Phys. Rev. Lett.* **92** 235003
[5] Evans T E et al 2005 *Nucl. Fusion* **45** 595–607
[6] Evans T E et al 2006 *Nat. Phys.* **2** 419–23
[7] Evans T E et al 2008 *Nucl. Fusion* **48** 024002
[8] Liang Y et al 2007 *Phys. Rev. Lett.* **98** 265004
[9] Kirk Aet al 2010 *Nucl. Fusion* **50** 034008
[10] Canik J M et al 2010 *Phys. Rev. Lett.* **104** 045001
[11] Suttrop W et al 2011 *Phys. Rev. Lett.* **106** 225004
[12] Jeon Y M et al 2012 *Phys. Rev. Lett.* **109** 035004
[13] Sun Y et al 2016 *Phys. Rev. Lett.* **117** 115001
[14] Nazikian R et al 2015 *Phys. Rev. Lett.* **114** 105002
[15] Paz-Soldan C et al 2015 *Nucl. Fusion* **55** 083012
[16] Park J-K et al 2018 *Nat. Phys.* **14** 1223
[17] Lanctot M J et al 2013 *Nucl. Fusion* **53** 083019
[18] Wade M R et al 2015 *Nucl. Fusion* **55** 023002
[19] Hu Q M et al 2021 *Phys. Plasmas* **28** 052505
[20] In Y et al 2019 *Nucl. Fusion* **59** 056009
[21] In Y et al 2019 *Nucl. Fusion* **59** 126045
[22] Kim M et al 2020 *Phys. Plasmas* **27** 112501
[23] Suttrop W et al 2018 *Nucl. Fusion* **58** 096031
[24] Sun Y et al 2017 *Nucl. Fusion* **57** 036007
[25] Gu S et al 2019 *Nucl. Fusion* **59** 126042
[26] Nazikian R et al 2014 Advances in the understanding of ELM suppression by resonant magnetic perturbations (RMPs) in DIII-D and implications for ITER 25th IAEA Int. Conf. on Fusion Energy (St Petersburg, Russia, 2014) EX/1-1
[27] Paz-Soldan C et al 2019 *Nucl. Fusion* **59** 056012
[28] Suttrop W et al 2016 *Plasma Phys. Control. Fusion* **59** 014049
[29] Fenstermacher M E et al 2008 *Phys. Plasmas* **15** 056122
[30] Joseph I et al 2008 *Nucl. Fusion* **48** 045009
[31] Schmitz O et al 2009 *Phys. Rev. Lett.* **103** 165005
[32] Kirk A et al 2011 *Plasma Phys. Control. Fusion* **53** 065011
[33] Liu Y et al 2011 *Nucl. Fusion* **51** 083002
[34] Ryan D A et al 2015 *Plasma Phys. Control. Fusion* **57** 095008
[35] Liu Y et al 2016 *Plasma Phys. Control. Fusion* **58** 114005

[36] Paz-Soldan C et al 2015 *Phys. Rev. Lett.* **114** 105001
[37] Logan N C et al 2016 *Phys. Plasmas* **23** 056110
[38] Ryan D A et al 2018 *Plasma Phys. Control. Fusion* **60** 065005
[39] Logan N C et al 2018 *Nucl. Fusion* **58** 076016
[40] Bécoulet M et al 2014 *Phys. Rev. Lett.* **113** 115001
[41] Orain F et al 2017 *Nucl. Fusion* **57** 022013
[42] McKee G R et al 2013 *Nucl. Fusion* **53** 113011
[43] Leconte M and Diamond P H 2012 *Phys. Plasmas* **19** 055903
[44] Hu Q M et al 2019 *Phys. Plasmas* **26** 120702
[45] Hu Q M et al 2020 *Nucl. Fusion* **60** 076001
[46] Hu Q M et al 2020 *Phys. Rev. Lett.* **125** 045001
[47] Fitzpatrick R 2020 *Phys. Plasmas* **27** 042506
[48] Fitzpatrick R 2020 *Phys. Plasmas* **27** 102511
[49] Park J et al 2009 *Phys. Rev. Lett.* **102** 065002
[50] Evans T E et al 2013 *Nucl. Fusion* **53** 093029
[51] Zhou L et al 2018 *Nucl. Fusion* **58** 076025
[52] Park J-K and Logan N C 2017 *Phys. Plasmas* **24** 032505
[53] Yu Q and Günter S 2011 *Nucl. Fusion* **51** 073030
[54] Snyder P B et al 2012 *Phys. Plasmas* **19** 056115
[55] Li L et al 2017 *Plasma Phys. Control. Fusion* **59** 044005
[56] Li L et al 2019 *Nucl. Fusion* **60** 016013
[57] Fitzpatrick R 1998 *Phys. Plasmas* **5** 3325
[58] Park J et al 2007 *Phys. Rev. Lett.* **99** 195003
[59] Park J-K et al 2009 *Phys. Plasmas* **16** 082512
[60] Park J et al 2007 *Phys. Plasmas* **14** 052110
[61] Yang S M et al 2020 *Nucl. Fusion* **60** 096023
[62] Park J-K et al 2011 *Nucl. Fusion* **51** 023003
[63] Logan N C et al 2016 *Nucl. Fusion* **56** 036008
[64] Wang Z et al 2014 *Phys. Plasmas* **21** 042502
[65] King J D et al 2015 *Phys. Plasmas* **22** 072501
[66] Logan N et al 2021 *Nucl. Fusion* **61** 076010
[67] Logan N C et al 2020 *Nucl. Fusion* **60** 086010
[68] Park J-K et al 2021 *Phys. Rev. Lett.* **126** 125001
[69] Yu Q, Günter S and Scott B D 2003 *Phys. Plasmas* **10** 797
[70] Yu Q 2010 *Nucl. Fusion* **50** 025014
[71] Waelbroeck F L et al 2012 *Nucl. Fusion* **52** 074004
[72] Günter S et al 2005 *J. Comput. Phys.* **209** 354
[73] Yu Q et al 2019 *Nucl. Fusion* **59** 106053
[74] Breslau J, Gorelenkova M, Poli F, Sachdev J and Yuan X 2018 *TRANSP v18.2. Computer Software.*
[75] Poli F M 2018 *Phys. Plasmas* **25** 055602
[76] Hu Q et al 2020 *Nucl. Fusion* **60** 076006
[77] Mordijck S et al 2012 *Phys. Plasmas* **19** 056503
[78] Hager R et al 2020 *Phys. Plasmas* **27** 062301
[79] Private communication with R. Nazikian on DIII-D observations.
[80] Gu S, et al, 2019 *Nucl. Fusion* **59** 026012
[81] Haskey S R et al 2018 *Plasma Phys. Control. Fusion* **60** 105001
[82] Nazikian R et al 2021 *Nucl. Fusion* **61** 044001
[83] Kotschenreuther M et al 2017 *Nucl. Fusion* **57** 064001
[84] Ashourvan A et al 2019 *Phys. Rev. Lett.* **123** 115001